Propagating Wigner-Negative States Generated from the Steady-State Emission of a Superconducting Qubit

Yong Lu[*], Ingrid Strandberg, Fernando Quijandría, Göran Johansson,[†] Simone Gasparinetti, and Per Delsing[‡]

Department of Microtechnology and Nanoscience MC2, Chalmers University of Technology,
SE-412 96 Göteborg, Sweden

We experimentally demonstrate the steady-state generation of propagating Wigner-negative states from a continuously driven superconducting qubit. We reconstruct the Wigner function of the radiation emitted into propagating modes defined by their temporal envelopes, using digital filtering. For an optimized temporal filter, we observe a large Wigner logarithmic negativity, in excess of 0.08, in agreement with theory. The fidelity between the theoretical predictions and the states generated experimentally is up to 99%, reaching state-of-the-art realizations in the microwave frequency domain. Our results provide a new way to generate and control nonclassical states, and may enable promising applications such as quantum networks and quantum computation based on waveguide quantum electrodynamics.

In the continuous-variable (CV) approach to quantum information processing [1,2], information can be represented by a phase space quasiprobability distribution such as the Wigner function [3]. To obtain a quantum computational advantage with a CV quantum circuit, either the input state, the circuit itself, or the final measurement needs to be characterized by a negative quasiprobability distribution [4]. For example, Gaussian boson sampling [5,6] utilizes Wigner-positive input states and a linear circuit, but has photon-number resolving detectors which are associated with Wigner-function negativity [7]. In this work, we focus on generating Wigner-negative states that could be used as a computational resource in a linear circuit with heterodyne or homodyne measurements.

Nonclassical states with negative Wigner functions have been implemented using natural atoms [8,9], trapped ions [10,11], and optical photons [12]. In superconducting quantum circuits, some Wigner-negative states have been implemented in 3D cavities [13–15] and resonators [16–18] where the states are stored in the confined modes of the cavities. Such states have a limited lifetime and the corresponding setups are relatively complicated. In waveguide quantum electrodynamics by using superconducting circuits, single photons as well as cat states have been generated and transferred [19–21]. These propagating states are generated by either releasing a cavity state or by exciting a quantum emitter that subsequently decays into a waveguide. However, in both cases, the states result from transient dynamics so that resetting the system after a

certain time is necessary. A continuously driven source may lead to higher generation rates, but the question whether Wigner-negative states can be generated this way has been theoretically addressed only recently [22,23], and experimental verification was still lacking. In Ref. [24] a qubit in an *infinite* waveguide was used to demonstrate photon antibunching or nonclassical correlations between photons emitted by the qubit. While that is a nonclassical phenomenon, the Wigner function of any propagating mode would be positive since the emitted field is in a mixed state [22].

In this work, we experimentally demonstrate the generation of Wigner-negative states using the steady-state emission from a continuously driven superconducting qubit. We study the nonclassical properties of the quantum state of light propagating along a *semi-infinite* waveguide, occupying the single mode defined by a temporal filter. We reconstruct the Wigner function of the state, and investigate the effect of different temporal mode filters. Our flux-tunable transmon qubit [25] is capacitively coupled to the open end of a one-dimensional transmission line [Figs. 1(a) and 1(b)]. The circuit is equivalent to an atom in front of a mirror in 1D space with a negligible distance between the qubit and the mirror. In this work, the qubit is operated at zero external flux.

The total scattered field from the qubit in front of a mirror is characterized by its annihilation operator a_{out} which contains two contributions: the incoming field operator a_{in} reflected by the mirror and the field emitted by the qubit, according to [36,37]

$$a_{out}(t) = a_{in}(t) - i\sqrt{\Gamma_r e^{i\phi}}\sigma_-(t), \qquad (1)$$

where $a_{in}(t) = \Omega(t)/(2\sqrt{\Gamma_r e^{i\phi}})$, Γ_r is the decay rate of the qubit into the transmission line, $\Omega(t)$ is the Rabi frequency
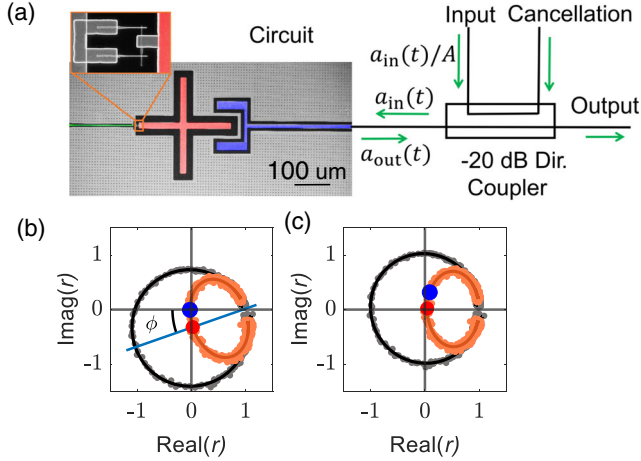
FIG. 1. Measurement setup and spectroscopy of a transmon qubit. (a) A simplified schematic of the measurement setup. Dir.Coupler denotes a directional coupler with coupling factor $A = 0.1$. $a_{in}(t)$ and $a_{out}(t)$ are the input and output signals. A superconducting circuit is connected to the directional coupler, where a transmon consisting of a superconducting island (red) shunted by a Superconducting QUantum Interference Device (SQUID) loop is capacitively coupled to a coplanar waveguide (blue) and inductively coupled to a flux line (green). The inset shows a close-up of the SQUID loop. (b) Single-tone spectroscopy, showing real and imaginary parts of the reflection coefficient r of a probe with the qubit at zero external flux. The black and orange dots are the experimental data of the reflection coefficient at two different intensities of the probe, namely, $\Omega \ll \Gamma_r$ and $\Omega \approx 0.707\Gamma_r$, respectively. The solid curves show the corresponding fittings to theory. (c) Here, the data in (c) has been corrected for the impedance mismatch in the probe line [26].

of the coherent input, the phase ϕ quantifies the impedance mismatch in the line (for a perfectly matched line, $\phi = 0$; see the Supplemental Material [26]), and $\sigma_-(t)$ is the qubit lowering operator.

To characterize the device, we apply a coherent continuous probe to the input port in Fig. 1(a). An input signal $a_{in}(t)$ reaches the qubit. The scattered field $a_{out}(t)$ is measured at the output port. In the steady state, the expectation value of $\langle a_{out}(t)\rangle$ is constant. By taking averages, we obtain the complex reflection coefficient as $r = \langle a_{out}\rangle/\langle a_{in}\rangle$ [Fig. 1(b), black dots]. By fitting data to the theory [Fig. 1(b), black line], we obtain $\phi = -0.319 \pm 0.03$, $\Gamma_r/2\pi = 1.11$ MHz and $\Gamma_2/2\pi = 0.528$ MHz, where Γ_2 is the total decoherence rate of the qubit. After compensating for the impedance mismatch, a parametric plot of the reflection coefficient describes a circle in the IQ plane [Fig. 1(c)]. The radius of the circle approaches unity, which implies than nonradiative decay and pure dephasing are negligible in our sample.

For a coherently driven two-level system in our mirror-like geometry, the largest Wigner negativity is expected when driving on resonance and choosing the drive power so that the coherent reflection vanishes [23]. This effect,

reported in previous experiments [38], is due to destructive interference between the radiation reflected by the mirror and the radiation coherently scattered by the two-level system. Here, we also find that at this drive power the coherence between the qubit's ground and excited states is maximized [26]. We call this power the critical power. In our case, due to the impedance mismatch, full cancellation is achieved at a slightly detuned driving frequency [by 170 kHz, blue circle in Fig. 1(b)]. By contrast, resonant driving of the system at the same power gives some residual coherent reflection [red circle in Fig. 1(b), caused by the impedance mismatch], which we eliminate in the measurements below by applying a cancellation pulse to the cancellation port of the directional coupler [Fig. 1(a)]. As we show in the following, both on- and off-resonant cases give comparable results with regards to the observed Wigner negativity.

The emission from the qubit is not confined and comprises a continuum of modes described by the operator $a_{out}(t)$. Here we study the quantum state occupying the single mode a defined by the filter function $f(t)$. Consequently, the properties of the state will depend on the chosen $f(t)$. We perform a full tomography of propagating modes, by measuring their statistical moments $\langle a^{\dagger m}a^n\rangle$, $m, n = 0, \ldots, N_c$, where $a = \int_0^\infty dt f(t)a_{out}(t)$ [39] and N_c is the photon-number cutoff. In order to excite the qubit, we send a long pulse 4.4 μs, much longer than the lifetime of the qubit, $T_1 = 1/\Gamma_1 = 145$ ns. This in order to ensure that the qubit has reached the steady-state before we perform the measurement of its emission field [26]. First, we consider a normalized rectangular boxcar filter which is a constant function within the time interval from $t_0 = 2.5$ μs to $t_0 + \tau/\Gamma_2$ and zero elsewhere. In Fig. 2 we show the magnitude of the moments up to 6th order
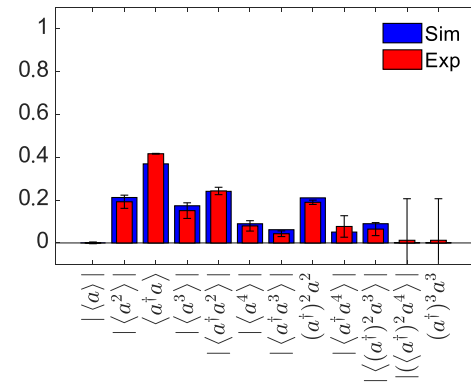

FIG. 2. Moments for the on-resonance case. Different orders of moments for the propagating state from the qubit emission with the measurement time window $\tau = 2.0$, where τ defines the length of the boxcar filter in the time domain. The red rectangles correspond to experimental data, which include the impedance mismatch in the line. The blue rectangles correspond to a numerical simulation of the ideal line, without the impedance mismatch.

($m + n \leq 6$) for $\tau = 2$ for the on-resonant case in red rectangles. Because of the small average photon number $\langle a^\dagger a \rangle$, it is enough to truncate the Fock space up to $N_c = 4$. Our results are very similar to the numerical simulations [40], using the method presented in Ref. [41] which correspond to the blue rectangles. The slight difference is due to the impedance mismatch which gives a higher Rabi frequency $\Omega_m = (0.74 \pm 0.01)\Gamma_1$ [26] than the ideal case $\Omega_m = 0.707\Gamma_1$, leading to a slightly larger photon number $\langle a^\dagger a \rangle$. Finally, as expected, the first order moment $\langle a \rangle$ is almost zero due to the additional pulse that corrects the effect from the impedance mismatch.

To demonstrate the nonclassical character of the generated states we now turn to their Wigner functions. We first extract the density matrix ρ of the filtered output from the measured moments using maximum likelihood estimation [42]. Then, we obtain the Wigner function from the relation $W(\alpha) = (2/\pi)\text{Tr}[\hat{D}(\alpha)\rho\hat{D}^\dagger(\alpha)\hat{\Pi}]$, where $\hat{D}(\alpha)$ is the displacement operator with amplitude α and $\hat{\Pi}$ is the parity operator [39]. In Fig. 3(a), the nonclassical nature of the outgoing field is corroborated by the negative values of the Wigner functions for different values of τ. As seen in the plots, with increasing τ from 0.5 to 2.0, the negativity region becomes larger. For $\tau > 2.0$, the corresponding negativity is decreased, as will be discussed below.

To quantify the nonclassical content of the state, we use the Wigner logarithmic negativity [43] defined as $\text{WLN} = \log\left(\int d\alpha |W(\alpha)|\right)$, which has the property $\text{WLN} > 0$ when the Wigner function $W(\alpha)$ has a negative part.

We calculate the WLN for both on- and off-resonant cases for the boxcar filter (red and blue markers, respectively) in Fig. 4(a). We see that the WLN increases when τ is increased from 0 to 2.1, whereas it starts to decrease when τ is increased further. Our experimental results

(markers in Fig. 4) are in excellent agreement with numerical simulations (solid lines) [44]. Since the chosen filter function defines the observed mode it is reasonable to expect that a different choice of filter function will also affect the observed negativity of the Wigner function [Figs. 3(a) and 3(b)]. In Fig. 4(b), we show the values of WLN for a measurement with a normalized Gaussian filter $f(t) = \sqrt{\Gamma_2}\exp(-t^2\Gamma_2^2/4\xi^2)/(2\pi\xi^2)^{1/4}$. Compared to the boxcar filter, the Gaussian filter with a width given by $\xi = 0.5$ can produce a state with a maximum WLN twice as large, which is also seen by comparing Fig. 3(b) and Fig. 3(a). Through numerical optimization we have verified that the Gaussian filter is indeed the optimal filter for maximizing the Wigner negativity, the same method is also used in Ref. [45].

From Eq. (1), the effect of the driving field on the total output is to displace the emission from the qubit. A displacement operation in phase space amounts to a translation of the Wigner function which does not affect its negativity. Therefore, in order to obtain the field emitted by the qubit, we can remove the coherent signal from the drive by means of a digital displacement with the opposite sign on the extracted density matrix of the total emission. Since we know the Rabi frequency Ω_m at the critical power, we can obtain the displacement as $(\Omega_m/2\sqrt{\Gamma_r/\Gamma_2})\sqrt{\tau}$. Therefore, we can obtain the photon number from the qubit emission in Fig. 4(c). This figure reveals the relation between the WLN and the single-photon population. For filtering times much smaller than the qubit decay time ($\tau \ll 1$), the field is approximately in the vacuum state, i.e., a Gaussian state and consequently, a Wigner positive state. As we increase τ, the single-photon population becomes non-negligible. In fact, for $0 \leq \tau \leq 1$, the state is mostly a superposition of the vacuum and single-photon states. As shown in Refs. [22,23], in this two-dimensional space, the
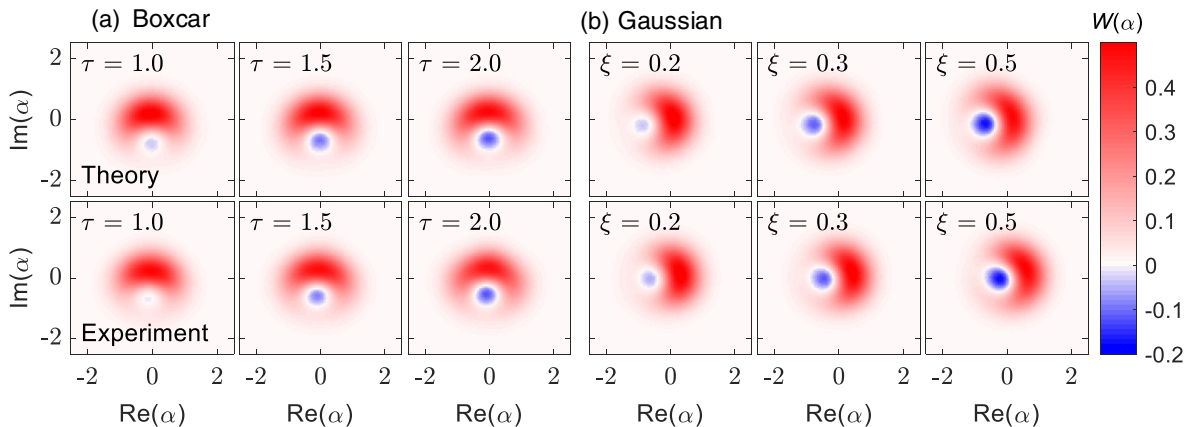

FIG. 3. Reconstructed Wigner function with boxcar and Gaussian filters. Comparison between the numerical simulation and the experiment for Wigner functions of the propagating states. Wigner functions for (a) the on-resonance case using a boxcar filter of length τ/Γ_2. (b) The off-resonance case using a Gaussian filter of standard deviation ξ/Γ_2. The negative values indicate that the states are nonclassical. The color scale has been adjusted to the measured data range for optimal visibility. The rotation between (a) and (b) is due to the phase of the driving field.
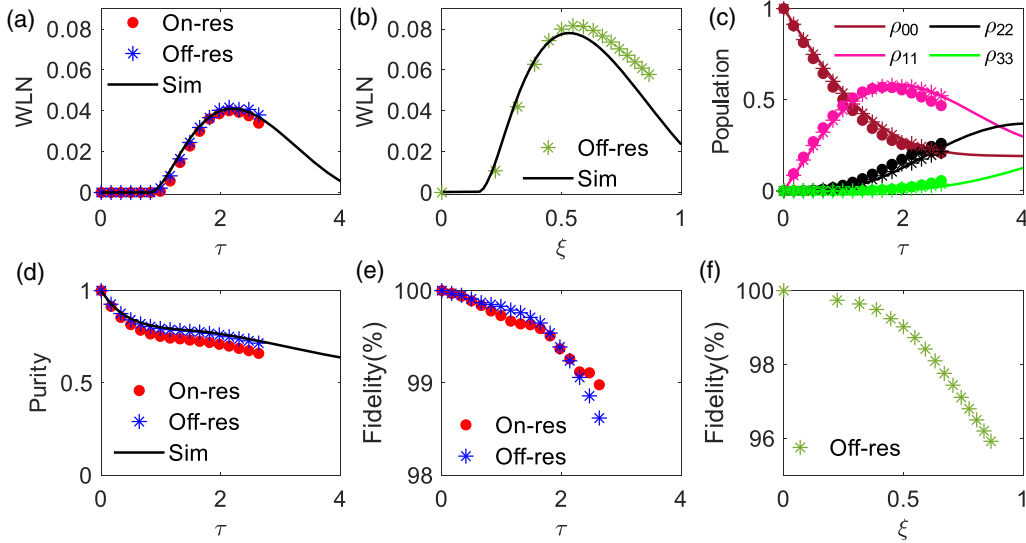
FIG. 4. Wigner logarithmic negativity (WLN), photon number content, and purity with different filters. These are obtained from the reconstructed density matrix ρ of the filtered output field using maximum likelihood estimation. In all panels, the markers are from the experiment whereas the solid curves are from the numerical simulation. On/Off-res and Sim represent the on- or off-resonant cases and the numerical simulation, respectively. (a) WLN with different τ values for a boxcar filter. The red and blue markers are for the on- and off-resonant cases, respectively. (b) WLN with different ξ values of the standard deviation of a Gaussian filter. (c) Photon populations for data shown in (a). ρ_{nn} are the diagonal elements of the density matrix and thus present the population of the photon number n of the emission field. (d) Photon purity for data shown in (a). The purity is given by $\mathrm{Tr}(\rho^2)$. (e) and (f) The corresponding fidelities between experimental and numerical results for the states used in (a) and (b), respectively. The fidelities are calculated according to $F = \mathrm{Tr}\sqrt{\sqrt{\rho^{1/2}\rho_{\mathrm{sim}}\rho^{1/2}}}$, where ρ_{sim} is the numerical density matrix.

relation between Wigner negativity and single-photon content strongly depends on the purity. In simple terms, for a statistical mixture of vacuum and a single photon, we require an average population of at least half a photon in order for the state to be Wigner negative. This required population decreases with an increasing purity. By comparing Figs. 4(a) and 4(c), we see that the WLN becomes nonzero roughly when the vacuum and the single-photon populations become identical at $\tau \simeq 1$.

For $\tau \geq 1$, two- and three-photon states in Fig. 4(c) are no longer negligible. Nevertheless, the single-photon population becomes the dominant contribution to the state. In fact, the WLN achieves its largest value when the single-photon state achieves its largest population ($\rho_{11} \approx 2\rho_{00}$ and $\rho_{11} \approx 4\rho_{22}$) at $\tau \simeq 2$.

Increasing τ further beyond the qubit decay time, the output field will contain more uncorrelated emissions. As it can be seen in Fig. 4(d), the net effect of this is to reduce the purity of the output state and consequently the Wigner negativity.

Because of the impedance mismatch, the Rabi frequency for the on-resonant case is slightly higher than the off-resonant case, resulting in a lower purity compared to the off-resonant case [Fig. 4(d)]. Accordingly, the corresponding WLN is smaller [Fig. 4(a)].

The single photon population and the purity of the state are higher for a Gaussian than for a boxcar filter, leading to a higher negativity [Figs. 4(a), 4(b) and Ref. [26]]. With a

larger filter width, the photon population is increased, this will lead to a non-negligible contribution from higher order moments. The measurement of these is limited by the system noise. Nevertheless, lower order moments still yield the dominant contribution to the field state. Therefore, the observed tendency of the WLN for $\xi > 0.5$ in Fig. 4(b) is in agreement with the numerical simulations.

Our nonclassical states have above 95% fidelities between the experimentally produced states and the predicted states for both types of filters with different lengths [Figs. 4(e) and 4(f)]. Especially, at maximum values of WLN, the fidelities are 99.24% and 99.05% for the boxcar and Gaussian filters, respectively.

Numerically, we find that our nonclassical state is much more sensitive to pure dephasing compared to nonradiative decay. Such a nonclassical state with biased noise may be useful for quantum computation [46]. Even though we do not investigate the frequency tunability of our nonclassical source by measuring the Wigner function at different qubit frequencies, it is still possible to estimate the pure dephasing and the nonradiative decay rates, and how much they affect the negativity. Our evaluation shows that the tunable bandwidth of our nonclassical source can be up to 400 MHz with negativities above 0.04 using a Gaussian filter [26].

Our setup provides a straightforward way to generate nonclassical states. Compared to pulsed operation [13–21,47], it has several advantages. (i) It has a higher

generation rate since the pulsed case requires to wait until the qubit returns to the ground state. (ii) We operate at the critical power, generating states with unit efficiency whereas in the pulsed scheme many photons are needed for the excitation pulse [20,21]. (iii) For a pulsed source there is a trade-off between high quantum efficiency and avoiding population of the higher levels of the qubit. In our case, the high-level excitation is negligible $\approx 10^{-5}$. (iv) Using our source in a quantum network, there is no timing requirement, the receiver can select any time slot of the continuous stream.

Our experimental results demonstrate that nonclassical states useful for quantum computation can be obtained from the steady-state dynamics of a continuously driven quantum system by applying optimized filters to its propagating output field. These conclusions can be extended to a variety of physical systems [48,49]. Recent theoretical work indicates that propagating Wigner-negative states may also be obtained from driven systems whose steady-state intracavity field is Wigner-positive, such as Kerr parametric oscillators [45]. This finding further broadens the class of systems to which the techniques shown here are applicable.

---

*yongl@chalmers.se
†goran.l.johansson@chalmers.se
‡per.delsing@chalmers.se

[1] N. C. Menicucci, Fault-Tolerant Measurement-Based Quantum Computing with Continuous-Variable Cluster States, Phys. Rev. Lett. **112**, 120504 (2014).

[2] M. Gu, C. Weedbrook, N. C. Menicucci, T. C. Ralph, and P. van Loock, Quantum computing with continuous-variable clusters, Phys. Rev. A **79**, 062318 (2009).

[3] K. E. Cahill and R. J. Glauber, Density operators and quasiprobability distributions, Phys. Rev. **177**, 1882 (1969).

[4] S. Rahimi-Keshari, T. C. Ralph, and C. M. Caves, Sufficient Conditions for Efficient Classical Simulation of Quantum Optics, Phys. Rev. X **6**, 021039 (2016).

[5] C. S. Hamilton, R. Kruse, L. Sansoni, S. Barkhofen, C. Silberhorn, and I. Jex, Gaussian Boson Sampling, Phys. Rev. Lett. **119**, 170501 (2017).

[6] Z. Han-Sen et al., Quantum computational advantage using photons, Science **370**, 1460 (2020).

[7] J. Hloušek, M. Ježek, and J. Fiurášek, Direct Experimental Certification of Quantum Non-Gaussian Character and Wigner Function Negativity of Single-Photon Detectors, Phys. Rev. Lett. **126**, 043601 (2021).

[8] B. Hacker, S. Welte, S. Daiss, A. Shaukat, S. Ritter, L. Li, and G. Rempe, Deterministic creation of entangled atom–light Schrödinger-cat states, Nat. Photonics **13**, 110 (2019).

[9] S. Deleglise, I. Dotsenko, C. Sayrin, J. Bernu, M. Brune, J.-M. Raimond, and S. Haroche, Reconstruction of nonclassical cavity field states with snapshots of their decoherence, Nature (London) **455**, 510 (2008).

[10] C. Monroe, D. Meekhof, B. King, and D. J. Wineland, A Schrödinger cat superposition state of an atom, Science **272**, 1131 (1996).

[11] C. Flühmann, T. L. Nguyen, M. Marinelli, V. Negnevitsky, K. Mehta, and J. P. Home, Encoding a qubit in a trapped-ion mechanical oscillator, Nature (London) **566**, 513 (2019).

[12] K. Makino, Y. Hashimoto, J.-i. Yoshikawa, H. Ohdan, T. Toyama, P. van Loock, and A. Furusawa, Synchronization of optical photons for quantum information processing, Sci. Adv. **2**, e1501772 (2016).

[13] Z. Leghtas et al., Confining the state of light to a quantum manifold by engineered two-photon loss, Science **347**, 853 (2015).

[14] P. Campagne-Ibarcq et al., Quantum error correction of a qubit encoded in grid states of an oscillator, Nature (London) **584**, 368 (2020).

[15] C. Wang et al., A Schrödinger cat living in two boxes, Science **352**, 1087 (2016).

[16] M. Hofheinz, E. M. Weig, M. Ansmann, R. C. Bialczak, E. Lucero, M. Neeley, A. D. O'Connell, H. Wang, J. M. Martinis, and A. N. Cleland, Generation of Fock states in a superconducting quantum circuit, Nature (London) **454**, 310 (2008).

[17] Y. Chu, P. Kharel, T. Yoon, L. Frunzio, P. T. Rakich, and R. J. Schoelkopf, Creation and control of multi-phonon Fock states in a bulk acoustic-wave resonator, Nature (London) **563**, 666 (2018).

[18] K. J. Satzinger et al., Quantum control of surface acoustic-wave phonons, Nature (London) **563**, 661 (2018).

[19] W. Pfaff, C. J. Axline, L. D. Burkhart, U. Vool, P. Reinhold, L. Frunzio, L. Jiang, M. H. Devoret, and R. J. Schoelkopf, Controlled release of multiphoton quantum states from a microwave cavity memory, Nat. Phys. **13**, 882 (2017).

[20] Z. Peng, S. De Graaf, J. S. Tsai, and O. Astafiev, Tuneable on-demand single-photon source in the microwave range, Nat. Commun. **7**, 12588 (2016).

[21] A. A. Houck et al., Generating single microwave photons in a circuit, Nature (London) **449**, 328 (2007).

[22] I. Strandberg, Y. Lu, F. Quijandría, and G. Johansson, Numerical study of Wigner negativity in one-dimensional steady-state resonance fluorescence, Phys. Rev. A **100**, 063808 (2019).

[23] F. Quijandría, I. Strandberg, and G. Johansson, Steady-State Generation of Wigner-Negative States in One-Dimensional Resonance Fluorescence, Phys. Rev. Lett. **121**, 263603 (2018).

[24] I.-C. Hoi, C. M. Wilson, G. Johansson, T. Palomaki, B. Peropadre, and P. Delsing, Demonstration of a Single-Photon Router in the Microwave Regime, Phys. Rev. Lett. **107**, 073601 (2011).

[25] J. Koch, T. M. Yu, J. Gambetta, A. A. Houck, D. I. Schuster, J. Majer, A. Blais, M. H. Devoret, S. M. Girvin, and R. J. Schoelkopf, Charge-insensitive qubit design derived from the Cooper pair box, Phys. Rev. A **76**, 042319 (2007).

[26] See Supplemental Material at http://link.aps.org/supplemental/10.1103/PhysRevLett.126.253602 for more details about the experimental setup, the impedance mismatch, and the results, which includes Refs. [27–35].

[27] C. Macklin, K. O'Brien, D. Hover, M. E. Schwartz, V. Bolkhovsky, X. Zhang, W. D. Oliver, and I. Siddiqi, A near–quantum-limited Josephson traveling-wave parametric amplifier, Science **350**, 307 (2015).

[28] P. Wen *et al.*, Large Collective Lamb Shift of Two Distant Superconducting Artificial Atoms, Phys. Rev. Lett. **123**, 233602 (2019).

[29] Y. Lu *et al.*, Characterizing decoherence rates of a superconducting qubit by direct microwave scattering, npj Quantum Inf. **7**, 35 (2021).

[30] M. Scigliuzzo, A. Bengtsson, J.-C. Besse, A. Wallraff, P. Delsing, and S. Gasparinetti, Primary Thermometry of Propagating Microwaves in the Quantum Regime, Phys. Rev. X **10**, 041054 (2020).

[31] J. M. Martinis *et al.*, Decoherence in Josephson Qubits from Dielectric Loss, Phys. Rev. Lett. **95**, 210503 (2005).

[32] J. Burnett *et al.*, Evidence for interacting two-level systems from the $1/f$ noise of a superconducting resonator, Nat. Commun. **5**, 4119 (2014).

[33] C. Müller, J. H. Cole, and J. Lisenfeld, Towards understanding two-level-systems in amorphous solids: Insights from quantum circuits, Rep. Prog. Phys. **82**, 124501 (2019).

[34] Y. Lu *et al.*, Quantum efficiency, purity and stability of a tunable, narrowband microwave single-photon source, arXiv:2105.11234.

[35] M. D. Hutchings, J. B. Hertzberg, Y. Liu, N. T. Bronn, G. A. Keefe, M. Brink, J. M. Chow, and B. L. T. Plourde, Tunable Superconducting Qubits with Flux-Independent Coherence, Phys. Rev. Applied **8**, 044003 (2017).

[36] B. Yurke and J. S. Denker, Quantum network theory, Phys. Rev. A **29**, 1419 (1984).

[37] C. W. Gardiner and M. J. Collett, Input and output in damped quantum systems, Phys. Rev. A **31**, 3761 (1985).

[38] I.-C. Hoi, A. F. Kockum, L. Tornberg, A. Pourkabirian, G. Johansson, P. Delsing, and C. M. Wilson, Probing the quantum vacuum with an artificial atom in front of a mirror, Nat. Phys. **11**, 1045 (2015).

[39] C. Eichler, D. Bozyigit, and A. Wallraff, Characterizing quantum microwave radiation and its entanglement with superconducting qubits using linear detectors, Phys. Rev. A **86**, 032106 (2012).

[40] J. R. Johansson, P. D. Nation, and F. Nori, Qutip: An open-source python framework for the dynamics of open quantum systems, Comput. Phys. Commun. **183**, 1760 (2012).

[41] A. H. Kiilerich and K. Mølmer, Input-Output Theory with Quantum Pulses, Phys. Rev. Lett. **123**, 123604 (2019).

[42] C. Eichler, D. Bozyigit, C. Lang, L. Steffen, J. Fink, and A. Wallraff, Experimental State Tomography of Itinerant Single Microwave Photons, Phys. Rev. Lett. **106**, 220503 (2011).

[43] F. Albarelli, M. G. Genoni, M. G. Paris, and A. Ferraro, Resource theory of quantum non-Gaussianity and Wigner negativity, Phys. Rev. A **98**, 052350 (2018).

[44] A. H. Kiilerich and K. Mølmer, Input-Output Theory with Quantum Pulses, Phys. Rev. Lett. **123**, 123604 (2019).

[45] I. Strandberg, G. Johansson, and F. Quijandría, Wigner negativity in the steady-state output of a Kerr parametric oscillator, Phys. Rev. Research **3**, 023041 (2021).

[46] P. Aliferis and J. Preskill, Fault-tolerant quantum computation against biased noise, Phys. Rev. A **78**, 052331 (2008).

[47] J.-C. Besse, S. Gasparinetti, M. C. Collodo, T. Walter, A. Remm, J. Krause, C. Eichler, and A. Wallraff, Parity Detection of Propagating Microwave Fields, Phys. Rev. X **10**, 011046 (2020).

[48] A. Laucht *et al.*, A Waveguide-Coupled on-Chip Single-Photon Source, Phys. Rev. X **2**, 011014 (2012).

[49] R. Katsumi, Y. Ota, M. Kakuda, S. Iwamoto, and Y. Arakawa, Transfer-printed single-photon sources coupled to wire waveguides, Optica **5**, 691 (2018).

Correction: The copyright license statement was presented incorrectly and has been fixed.